Catalyst-Free Photochemical Activation of Peroxymonosulfate in Xanthene-Rich Systems for Fenton-Like Synergistic Decontamination: Efficacy of Proton Transfer Process

Fanzhi Qin [a], Eydhah Almatrafi [b], Chen Zhang *[a], Danlian Huang [a], Lin Tang [a], Abing Duan [a], Deyu Qin [a], Hanzhuo Luo [a], Chengyun Zhou [a, b], Guangming Zeng *[a, b]

[a] Dr. F.Z. Qin, Prof. C. Zhang, Prof. D.L. Huang, Prof. L. Tang, Prof. A.B. Duan, Dr. D.Y. Qin, Dr. H.Z. Luo, Prof. C.Y. Zhou, Prof. G.M. Zeng
College of Environmental Science and Engineering and Key Laboratory of Environmental Biology and Pollution Control (Ministry of Education)
Hunan University
Changsha 410082, P.R. China
E-mail: zhangchen@hnu.edu.cn (C. Zhang); zgming@hnu.edu.cn (G.M. Zeng)

[b] Prof. E. Almatrafi, Prof. C.Y. Zhou, Prof. G.M. Zeng
Centre of Research Excellence in Renewable Energy and Power Systems, Center of Excellence in Desalination Technology, Department of Mechanical Engineering, Faculty of Engineering-Rabigh
King Abdulaziz University
Jeddah 21589, Saudi Arabia

Abstract: Catalyst-free visible light assisted Fenton-like catalysis offers opportunities to achieve the sustainable water decontamination, but the synergistic decontamination mechanisms are still unclear, especially the effect of proton transfer process (PTP). The conversion of peroxymonosulfate (PMS) in photosensitive dye-enriched system was detailed. The photo-electron transfer between excited dye and PMS triggered the efficient activation of PMS and enhanced the production of reactive species. Photochemistry behavior analysis and DFT calculations revealed that PTP was the crucial factor to determine the decontamination performance, leading to the transformation of dye molecules. The excitation process inducing activation of whole system was composed of low energy excitations, and the electrons and holes were almost contributed by LUMO and HOMO. This work provided new ideas for the design of catalyst-free sustainable system for efficient decontamination.

Introduction

Clean water and sanitation, one of the Sustainable Development Goals (SDGs), is one of the most severe challenges faced by the world today, especially in economically underdeveloped areas [1]. Advanced oxidation process (AOPs) mediated by sulfate radicals ($SO_4\cdot^-$), as a practical substitute for traditional decontamination contributed by hydroxyl radicals ($\cdot OH$), has attracted considerable attention [1b, 2]. $SO_4\cdot^-$ is generally produced by homolysis or heterolysis of O-O in persulfate. And peroxymonosulfate (PMS) is easier to be activated and has broader application prospects than peroxydisulfate (PDS) due to its asymmetric structure and higher reactivity [3]. Generally, persulfate can be activated by energy-transfer processes, for instance, ultraviolet radiation [4], thermal activation [2b] and ultrasonic activation [5]. Promoting the occurrence of electron transfer is the mainstream idea for persulfate activation at present, using reduced metals, transition metal oxides, mineral materials, carbonaceous materials, etc. [1a, 6]. Although these catalysts have achieved meaningful decontamination, they have significant disadvantages in suiting practical application, such as: i) leaching of metals and leakage of toxic substances to bring self-source pollution; ii) relatively expensive costs; and iii) potential risks of unexpected by-products [7]. Addressing these challenges has motivated intensive research on construction of efficient catalyst-free AOPs.

Catalyst-free visible light (VL) assisted PMS activation was sustainable and easy to operate without additional energy or external chemical consumption [3a]. However, in conventional direct photocatalytic systems, the activation efficiency of PMS induced by VL was extremely low due to the rapid recombination of photogenerated hole-electron pairs and the stability of O-O bonds [8]. Inspired by dye-sensitized photocatalysis systems, researchers have proposed that the strong absorption of chromophores in xanthene structures to visible region of solar spectrum could play a positive role in the generation of photoelectrons [9]. Thus, we speculated that the introducing of xanthene structures in AOPs could promote the efficient activation of PMS (as the photo-induced electron acceptor) under VL to enhance the production of reactive species (RS), and significantly improve the separation efficiency of hole-electron pairs, bringing synergistic effect to achieve decontamination. Xanthene structures are the matrix of most photosensitive dyes (PD), commonly existing in dyeing and food processing wastewater [10]. Therefore, using PMS to remove contaminants from PD-enriched wastewater under visible light is an attractive strategy of ‘treating waste with waste’, which can significantly strengthen the purification efficiency of wastewater simultaneously containing dye and other contaminations, realizing the sustainable utilization of water resources.

However, the application and understanding of dye-based PMS activation system under visible light are still limited, and the following problems remain unsolved: i) the excitation principles of dyes and the mechanisms of PMS activation promoted by dyes under VL are not clear; ii) how the molecular structures of dyes affect PMS activation has not been reported, and the protonation and intramolecular proton transfer process (PTP) may have crucial effects on system reactivity [11]; iii) little is known about the synergistic effect of photosensitive dyes and PMS on the degradation of other contaminations. Here, we have developed a new type of dye-based photo-responsive PMS activation (DPPA) system and comprehensively discussed the photosensitized activation of PMS in PD-enriched solution under simulated solar irradiation. The catalytic performance and photochemical behavior of DPPA system were explored systematically by experimental analysis and theoretical calculations, and it was confirmed that PTP was the key factor determining the reactivity of synergistic decontamination process mediated by DPPA system. And the intramolecular spirocyclization reaction (ISR) and de-spirocyclization reaction (IDR) of PD molecules were the core mechanisms causing changes of dominant excitation processes. Intriguingly, the impact of PTP on DPPA system exhibited a significant dual effect on key substances (i.e., PMS and dyes), and hole-electron analysis also indicated that the near-neutral environment helped photosensitive dyes to expose more regions of active photo-induced electrons. Finally, it was demonstrated that this new-type DPPA system used for synergistic decontamination can achieve great benefits in a wide range of pH.

Results and Discussion

It is impractical to achieve efficient catalyst-free activation of PMS induced by direct VL due to its high bond dissociation energy of O-O bond (377 kJ·mol^{-1}) [8, 12]. Therefore, erythrosine B (EB, a typical fluorescein derivative with xanthene structure) was chosen as the photosensitive substance to provide excellent capacity to absorb sunlight [11b]. To verify the promoting effect of EB photosensitization on PMS activation, the de-coloration of EB by different systems was systematically studied (Figure 1a). Although EB can be directly decomposed by 95.9 % under VL within 30 min, the introducing of PMS greatly accelerated this process. The direct photo-bleach of EB benefited from the networks of conjugated C-C bonds providing effective absorption of the longer wavelength light [13]. The residual content changes of PMS during reactions (Figure 1e and 1f) also showed that compared with the system without light, the consumption of PMS in the system activated by EB under VL increased 2.75 times. Thus, it could be preliminarily obtained that EB can photoactivate PMS under VL irradiation and achieve autocatalytic degradation.

In dye-sensitized H_2O_2 production system, the photocatalysis process was achieved based on the electron transfer between excited dye molecules (dye*) and semiconductors [9a]. So, we speculated that PMS activation by photoexcited dyes may also follow a similar electron-mediated process. To demonstrate the importance of photoexcited effects of dyes in PMS activation, the three-dimensional (3D) fluorescence spectra of EB system with or without PMS were monitored, focusing on their fluorescence emission intensity. Under natural conditions, EB and other dyes with photosensitive properties will have a spontaneous photoexcitation process. But because of the instability of excited state, dye* may soon emit energy and return to the ground state [14]. If the energy obtained is sufficient and the dye structure allows the excitation process based on charge transfer to occur, the production of active photo-induced electrons may happen due to prominent separation of hole-electron pairs (Eq. (1 - 3) in Text S1). The above processes coincidentally correspond to the excitation-emission spectra of dyes, so the change of fluorescence intensity is generally used as the sign of dyes happening intramolecular charge separation [15]. If PMS have captured free photoelectrons and achieved its own effective activation, then the recombination of EB^{*+} and electrons will be inhibited, showing a significant decrease in EB fluorescence emission intensity, which was verified in Figure S1. In addition, there was no obvious change in EB concentration before and after fluorescence measurement (Figure S2), further confirming that the decrease of fluorescence intensity was caused by electron transfer rather than self-degradation. And processes of EB activating PMS and auto-catalytic bleaching under VL may involve the following steps (Eq. (4 - 9) in Text S1). The above proved the feasibility of constructed EB-based DPPA system.

To evaluate the synergistic decontamination performance of DPPA system, tetracycline (TC) was selected as a model contaminant. The individual and synergistic degradation analysis of TC were systematically conducted (Figure 1b - 1d). VL, PMS, EB, PMS/VL or EB/VL alone could not effectively result in TC degradation. But when little PMS was introduced into EB/TC/VL system, it will cause a distinct increase in TC removal rate, showing efficient PMS activation. The removal of TC increased continuously with the increase of PMS concentration from 0.05 to 0.40 mM, but it was inhibited until exceeding 0.40 mM. Since the amounts of generated reactive oxygen species (ROS) and $SO_4^{\cdot-}$ were directly affected by PMS concentration, the significant decrease in oxidative activity under a higher PMS concentration may connect with the self-scavenging effect of excess ROS/$SO_4^{\cdot-}$ (Eq. (10 - 16) in Text S2) [8]. The UV-Vis full spectrum results of each reaction system also supported this phenomenon (Figure S3). When PMS concentration was moderate (0.40 mM), the residues of by-products were no longer obvious after 60 min reaction. While peaks of intermediate products would reappear when the concentration exceeded this level. Meanwhile, combined with experiment results of PMS residual concentrations (Figure S4, Figure 1e and 1f), it could be judged that 0.40 mM was the optimal oxidant dosage, and the utilization amounts of PMS were the highest (0.32 mM) and TC removal was the most sufficient. Moreover, the consumption law of EB was similar with the TC removal trend, indicating that TC and EB have been synergistically degraded in DPPA system.

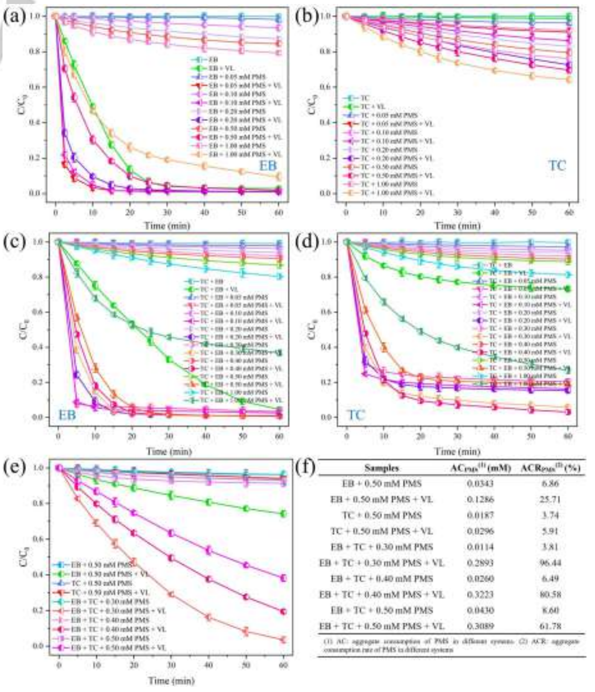

Samples	AC$_{PMS}$$^{(1)}$ (mM)	ACR$_{PMS}$$^{(2)}$ (%)
EB + 0.50 mM PMS	0.0343	6.86
EB + 0.50 mM PMS + VL	0.1286	25.71
TC + 0.50 mM PMS	0.0187	3.74
TC + 0.50 mM PMS + VL	0.0296	5.91
EB + TC + 0.30 mM PMS	0.0114	3.81
EB + TC + 0.30 mM PMS + VL	0.2893	96.44
EB + TC + 0.40 mM PMS	0.0260	6.49
EB + TC + 0.40 mM PMS + VL	0.3223	80.58
EB + TC + 0.50 mM PMS	0.0430	8.60
EB + TC + 0.50 mM PMS + VL	0.3089	61.78

(1) AC: aggregate consumption of PMS in different systems. (2) ACR: aggregate consumption rate of PMS in different systems

Figure 1. De-coloration efficiency of EB (a, c), removal efficiency of TC (b, d) and residue change of PMS (e, f) in different reaction systems. Conditions: $[PMS]_0 = 0.05 \sim 1.00$ mM, $[EB]_0 = 0.02$ mM, $[TC]_0 = 10$ mg/L and $\lambda > 420$ nm irradiation.

Surprisingly, from the perspective of reaction rate, the effect of PMS concentration seemed to be negative all the time. Although the existence of PMS brought the gain of TC removal, the increase of PMS concentration also continuously suppressed the reaction rate in DPPA system (see the reaction trends in Figure 1a, 1c and 1d). This cannot simply be attributed to self-quenching effects among reactive species. Notably, we have noticed that in the UV-Vis full spectra, with the increasing of PMS concentration, the maximum absorption peak of EB original solution decreased continuously, showing a hypochromic effect. In this study, PMS was added in the form of $KHSO_5 \cdot 0.5KHSO_4 \cdot 0.5K_2SO_4$, so the DPPA system would be acidified. And the higher the concentration of PMS was, the smaller the pH of the system was. Herein, we guessed that the PTP has occurred in the research system, and structures and properties of EB were prominently affected by protonation processes, exhibiting a strong proton transfer dependence. DPPA may be a pH-dependent system, and pH will affect its photo-response activity, thus regulating the production of reactive species.

As a typical fluorescein derivative, the photochemical properties of EB molecule in solution mostly depend on its structure [16]. The pH is potentially a critical variable for the transformation of EB structure, leading to PTP. Since the original EB molecule (marked as $[EB]^{2-}$) possesses two concentrated negative charges, at most twice protonation can easily occur in its structure, forming $H[EB]^-$ and $H_2[EB]$, respectively. However, when the proton concentration in solution is at a high level, $H_2[EB]$ may also continue to accept a proton, resulting in a third-order protonation process ($H_3[EB]^+$) [17]. Notably, it is not clear in which site each-order protonation of EB occurs, nor how the introduced proton will affect its structures and properties. In order to clarify the effects of PTP on properties of EB, the possible structures of EB under different degrees of protonation were calculated based on density functional theory (DFT), and the Mulliken charge and Hirshfeld charge distribution [18] of each structure were studied, as shown in Figure S5, Table S1 and S2.

The dianion structure of EB is generally uncontroversial, mainly in the form of carboxylate [10b]. In the charge distribution analysis of $[EB]^{2-}$, O27, O28, O29 and O31 showed the most concentrated charge and were more inclined to accept the first proton. Moreover, O27/O29 and O28/O31 were equivalent in geometrical configuration, so $H[EB]^-$and $H[EB]_p^-$ (Figure S5) were the most likely monoanionic structures of EB. Meanwhile, analysis about their charge distribution also showed that after introduction of the first H^+, $H[EB]^-$ dispersed the negative charge concentrated in molecule (O27 ~ O31) and reduced the intramolecular repulsion, having greater configuration advantages than $H[EB]_p^-$. In addition, the electronic energies and thermodynamic quantities of EB in different states were calculated (Table S3). From the view of energy, $H[EB]^-$ also had the lower energy state and higher thermodynamic stability than $H[EB]_p^-$, thus it was identified as the main product after first-order protonation. Similarly, the second-order protonation process was analysed. Due to the equivalence of O29 and O31, $H_2[EB]_p$ seemed to be the only reasonable structure of neutral form. However, we have found that the introduction of the second proton also made C7 to show more positive electricity, which strengthened its electrostatic attraction towards adjacent O28. Combined with the study about fluorescein molecule by Li et al. [19], we speculated that second-order protonation of EB might cause a intramolecular PTP from O27 to O31, resulting in the intramolecular esterification, calling ISR in this study. The produced ISR product was proved to be colourless and weakly fluorescent [20], which was coincided with the phenomenon in Figure S3. Notably, there was no obvious difference in thermodynamic stability between $H_2[EB]$ and $H_2[EB]_p$. However, the charge distribution indicated that $H_2[EB]$ structure was not only more conducive to charge dispersion of negative centers, but also stabilized intramolecular protons (H36 ~ H37), possessing more significant structural advantages. So, it was proved that $H_2[EB]$ was the main product of the second-order protonation. For the third-order protonation, there was no doubt that O27 was the preferred site. After accepting the third proton, due to the abrupt decline of negative charge in O28, the whole molecule would present a de-spirocyclization state (IDR), then forming $H_3[EB]^+$.

To verify the rationality of protonation process inference, the UV-Vis full spectra of EB solutions under various pH were monitored (Figure 2a and 2c). The decrease of pH did bring the hypochromic effect on EB solution. Before pH was reduced to 5.00, the hypochromicity was not obvious. When pH was lower than 5.00, the solution colour began to transform to light pink, and a huge colour change occurred especially in pH of 3.00 ~ 4.00. These were consistent with the trend of spirocyclization in protonation processes of EB. Surprisingly, the de-spirocyclization structure $H_3[EB]^+$, which recovered the fluorescence properties, was supposed to show distinct colour again, but in fact did not. This may be attributed to the slow process of the third-order protonation in practical solution, so the structure of ISR was basically maintained during detection, exhibiting light colour. Moreover, as $H_3[EB]^+$ showed a significant positive charge, the intermolecular electrostatic attraction or hydrogen bond structure would be generated, resulting in molecule self-aggregation, thus forming hydrophobic molecular clusters, which would precipitate and detach from the homogeneous solution system after a period of times (Figure 2b) [21]. The research of Snigur and co-workers [17] have supported our discussions above, and pK_a of $H_3[EB]^+$ in each-order ionization based on tristimulus colourimetry were given (3.50, 4.90 and 10.10, respectively). Synthesizing above explorations and previous studies about fluorescein structures [20, 22], we proposed the pathways of EB protonation processes and the detailed mechanisms of ISR and IDR (Figure 2d). And it was proved that the properties of EB showed a strong PTP dependence.

The influence of PTP on DPPA was macroscopically expressed as the impact brought by pH change, which can promote or inhibit the reactivity of key substances (PMS and EB) by changing their existing forms. Based on DFT, the frontier molecular orbital (FMO) distribution of each structure was calculated to analyze the effect of PTP on EB reactivity (Figure 3 and Figure S6). The results showed that with the enhancement of protonation, the energy difference between LUMO and HOMO of EB molecule was increasing, manifesting a continuous weakening trend of charge transfer and electron excitation. Although IDR process would restore fluorescence properties of EB, the effective concentration of EB in solution was significantly reduced due to the occurrence of self-aggregation. From the effect on existence forms of EB, decreasing pH was not conducive to its photosensitization processes in DPPA.

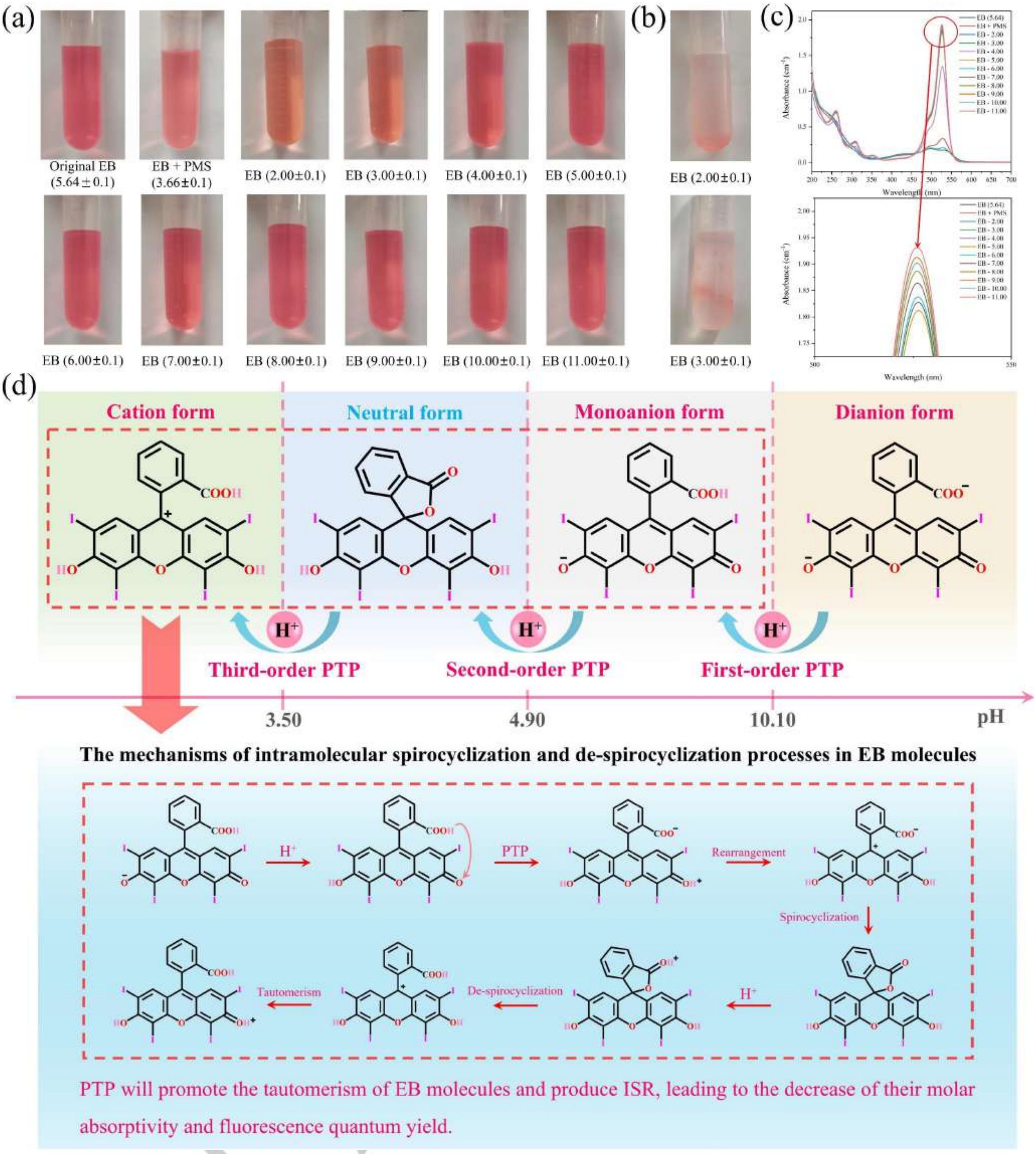

Figure 2. Colours of EB solutions (a) and solutions after standing for 30 min (b), as well as UV-Vis full spectrum tests (c) at different pH. Conditions: 200 ~ 700 nm, $[PMS]_0$ = 0.40 mM, $[EB]_0$ = 0.02 mM. And the proposed pathways of EB protonation processes and detailed mechanisms of ISR and IDR (d).

In order to get close to real photoactivation processes, the optical excitation properties of EB were also studied via time-dependent DFT (TDDFT). The information of ten excited states with the lowest energy in each structure was completely calculated to ensure the accuracy of calculations, mainly discussing the first six excited states (Table S4 and S5). The oscillator strength (*f*) between ground state and excited state have revealed the main tendency of excitation processes [23]. The calculation results showed that without considering ISR, the main excitation process of EB molecule gradually transitioned from $S_0 \rightarrow S_1$ to $S_0 \rightarrow S_2$ with the decreasing of pH, and the excitation energy increased continuously. The appearance of ISR also significantly weakened the visible light-responsive properties of DPPA system, and the excitation process turned into $S_0 \rightarrow S_6$ with the highest excitation energy. The overall trend of excitation properties was generally consistent with changes of HOMO-LUMO gap, indicating that the improvement of pH was helpful to the photosensitive processes of EB under VL.

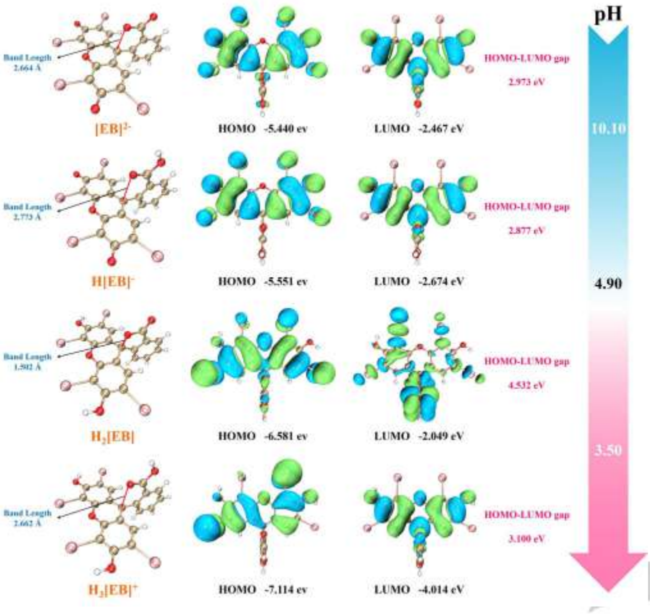

Figure 3. FMO distribution of EB molecule under various forms (isosurface value: 0.0200 a.u.). The blue and green represented the negative and positive phases of molecular orbitals, respectively.

In addition, the change of pH will also lead to the protonation and deprotonation of PMS structure, and then affect its affinity towards active photoelectrons [24]. Similarly, the structures of HSO_5^-, H_2SO_5 and SO_5^{2-} were analysed, as well as their FMO (Figure S7). Theoretically, PMS structure with the more negative LUMO level will exhibit stronger tendency as electron acceptor, possessing a higher activation efficiency [25]. The order of LUMO level was $SO_5^{2-} > HSO_5^- > H_2SO_5$, indicating acidic medium was more favourable for direct activation of PMS. The analysis results of charge distribution (Table S6) and orbital-weighted (OW) Fukui function ($f(\mathbf{r})$) (Table S7) about PMS structures also presented a similar trend. Text S3 explained the detailed definition of OW $f(\mathbf{r})$ and OW dual descriptor (DD) [26]. To further study the effect of PTP on cleavage of O-O bonds in PMS, the Gibbs free energy changes (ΔG) of direct homolysis of PMS in solution were calculated (Table S8 - S10). The breaking processes of O-O bonds of PMS in solution can be summarized as three paths (Eq. (17 - 19) in Text S4). The results revealed that with the protonation of PMS, the free energy needed to break O-O bond continued to decrease, which was theoretically beneficial to PMS activation.

Based on above discussions, it was not difficult to find that the influence of PTP on DPPA system was manifested as a significant dual effect on reactive substances. The intensification of protonation was not conducive to the photosensitization processes of EB, while enhanced deprotonation inhibited the activation of PMS and weakened its intramolecular stability [24b]. The acidic condition showed the negative effect on EB and the positive effect on PMS, while the alkaline condition was just the opposite. Therefore, the overall activity of DPPA system was inhibited under the strong alkali/acid conditions. The weak acid/alkali and neutral conditions were beneficial for this system to achieve efficient synergistic decontamination, which was consistent with the trend of influencing factor experiments about pH (Figure 4a - 4d). The optimal pH range after coordination of positive and negative effects was 5.00 ~ 6.00, which was in a relatively mild operating condition. Moreover, results also showed that DPPA system can all obtain high benefits in a wide range of pH (3.50 ~ 10.00). Although it was PTP-dependent, it had presented remarkable performance advantages, and was no need to introduce exogenous catalysts.

To explore the degradation principles of DPPA system, active species involved were identified comprehensively. For the photoactivation process of PMS, the changes of 7-hydroxycoumarin (7-HC) signal in DPPA system were monitored (Figure S8). Within 60 min of reaction, 7-HC signal produced and strengthened rapidly, verifying the existence of characteristic radical (·OH) and the continuous efficient activation of PMS. Further, the RS generated from photosensitized transformation in DPPA system were examined by electron spin resonance (ESR) with 5,5-dimethyl-1-pyrroline *N*-oxide (DMPO), 4-amino-2,2,6,6-tetramethylpiperidine (TEMP) and 2,2,6,6-tetramethylpiperidine-1-oxyl (TEMPO) as the spin trapping agents (Figure 5a - 5d) [3a]. The signal intensity of TEMPO decreased continuously with the extension of irradiation time, proving the generation of photogenerated EB^{*+}. Similarly, other detection results also presented corresponding characteristic peak spectra, indicating the production of target RS, and the signals gradually became obvious with time lapse. Compared with pure EB system, the abundance of RS after adding PMS increased significantly, and large numbers of RS were accumulated in 10 min, providing the possibility for rapid oxidation and mineralization of contaminants in a short time. After adding $K_2Cr_2O_7$ as the electron scavenger [27], signals of all kinds of RS manifested a weakened trend, exhibiting that electron transfer between EB and PMS was the key mechanism to induce and promote photosensitive activation processes in DPPA system.

For the purpose of clarifying the contribution of RS produced by DPPA system in decontamination, quenching experiments of each active specie were carried. Isopropanol (IPA), MeOH, $Na_2C_2O_4$, L-tryptophan (L-try) and 4-hydroxy-2,2,6,6-tetramethylpiperidine-1-oxyl (TEMPOL) were used as quenching agents for $SO_4^{\cdot-}$, compound radicals ($SO_4^{\cdot-}$ and ·OH), EB^{*+}, $^1O_2$ and $\cdot O_2^-$, respectively. As shown in Figure 5e and 5f, after quenching $\cdot O_2^-$ or $^1O_2$, TC removal was inhibited significantly. When IPA, MeOH and $Na_2C_2O_4$ existed in system, the degradation efficiency was reduced to 95.2 %, 92.8 % and 88.7 %, respectively. Moreover, EB consumption rate in quenching systems (except quenching EB^{*+}) also showed the similar inhibition trend as TC degradation rate. The apparent rate constants (k) displayed in Figure 5h reflected the photocatalytic degradation kinetics of TC in DPPA system, conforming to quasi-first order process. And the contributions of different RS to the reactivity of this system were calculated according to equations in Text S5 [28]. Notably, the total contribution of RS was significantly more than 100.0 %, mainly because the photosensitive activation processes involved very complex radical chemistry with mutual transformations among different RS [29]. Under reaction conditions, adding quenchers could not only inactivate the target RS, but also indirectly affect roles of other species by blocking transformations among RS, thus exhibiting a higher inhibition rate [30]. For further clearing the mechanisms of DPPA system, ESR tests of systems after adding $\cdot O_2^-$ /$^1O_2$ quenching agent were conducted (Figure S9). The results showed that after quenching $^1O_2$, the abundance of $^1O_2$ decreased significantly, and the signal of $\cdot O_2^-$ weakened slightly. While both $\cdot O_2^-$ and $^1O_2$ showed a significant decreasing trend after quenching $\cdot O_2^-$, so as to verify the mutual transformation. In addition, the signal changes of EB^{*+} and $\cdot OH/SO_4^{\cdot-}$ have also reflected the related effects, revealing the mutual transformations and interactions among RS. To sum up, in the process of TC degradation by DPPA system, the dominant active species were $\cdot O_2^-$ and $^1O_2$, followed by EB^{*+}, while $SO_4^{\cdot-}$ /$\cdot OH$ may mainly participate in mutual transformations among various RS and play roles in partially oxidizing process. To explore whether O_2 was another important factor affecting DPPA system, the photosensitive degradation experiments of TC were performed under continuous Ar/N_2/O_2 purge (Figure 4e and 4f). The results revealed that the decontamination ability of DPPA system was inhibited after the inert gas introduction, while the artificial increase of oxygen content strengthened its reactivity (Figure 5g and Table S11). Moreover, corresponding ESR tests were carried out to analyze the effects of O_2 content on related active species (Figure S10). It was proved that gas purging affected the molecular oxygen activation pathways by changing the dissolved oxygen (DO) content of DPPA system, and then enhanced/weakened the generation of related active species. Based on the above discussions, the main mechanisms of DPPA system were summarized in Text S6, and the photoexcitation of EB as well as electron/energy transfer from EB* have induced the activation of the whole system [24b, 31].

The core mechanism of DPPA system was proved to be electron transfer, and photo-induced electrons were mainly provided by photoexcitation process of EB, so it was necessary to discuss the activation initiation of EB in this system and the active sites in its molecular structures. Based on TDDFT simulation, the hole-electron distribution of dominant excitation processes of EB molecules was analyzed comprehensively. Hole-electron analysis described the electron excitation in a molecule as a process of electron transfer from ‘hole’ area to ‘electron’ area, and visually examined the origin, excitation destination and excitation characteristics of excited electrons [32]. The basic analysis results about hole-electron distribution were listed in Table S12, and Text S7 explained the meanings of main indicators. The excitation processes of IDR structures were dominated by local excitation (LE), performing partial characteristics of charge transfer excitation (CT) [33]. While due to the greater overlap between holes and electrons as well as the smaller centroid distance of hole-electron in charge transfer direction, the ISR structure of EB (i.e., $H_2[EB]$) showed more prominent LE characteristics with smaller exciton binding energy and higher recombination possibility of hole-electron pairs, and was not conducive to photo-induced excitation and conduction of electrons [34]. Figure 5i displayed the visual distribution of electrons and holes, and pink arrows revealed the direction of electron excitation transfer. Obviously, for IDR structures (mainly $[EB]^{2-}$ and $H[EB]^-$), the low-energy excitations, including $\pi \rightarrow \pi^*$ with large conjugated systems and $n \rightarrow \pi^*$ etc., constituted the main excitation process, showing the absorption characteristics of near ultraviolet and visible light (long wave absorption). While in excitation process of ISR structure, the general $\pi \rightarrow \pi^*$ process was dominated, manifesting the absorption characteristics of ultraviolet band (short wave absorption), which was not beneficial to DPPA system functioning under visible light and with fewer active photoelectron regions exposed.

As the distribution of holes and electrons was complex in most cases, the highly smoothed C_{hole} and C_{ele} functions, which were alike to Gaussian functions in function behavior, were introduced to analyze their concentrating states more intuitively [35]. As depicted in Figure 5j, during the excitation processes of EB, the ‘electron’ region and ‘hole’ region were mainly distributed along lateral spreading, and electrons in molecules overall exhibited a bottom-up excitation trend. The concentration area of active photoelectrons in each excitation process was highlighted by the blue dotted lines, representing the sites capturing electrons by electron acceptors. In $S_0 \rightarrow S_6$ process of $H_2[EB]$, the ‘hole’ region almost covered the whole ‘electron’ region, presenting a weak ability of electron transfer. Additionally, the contributions of molecular orbitals and key atoms to electrons and holes (Table S13 - S14, and Figure S11 - S12) were quantitatively studied to determine the reactivity origin of DPPA system.

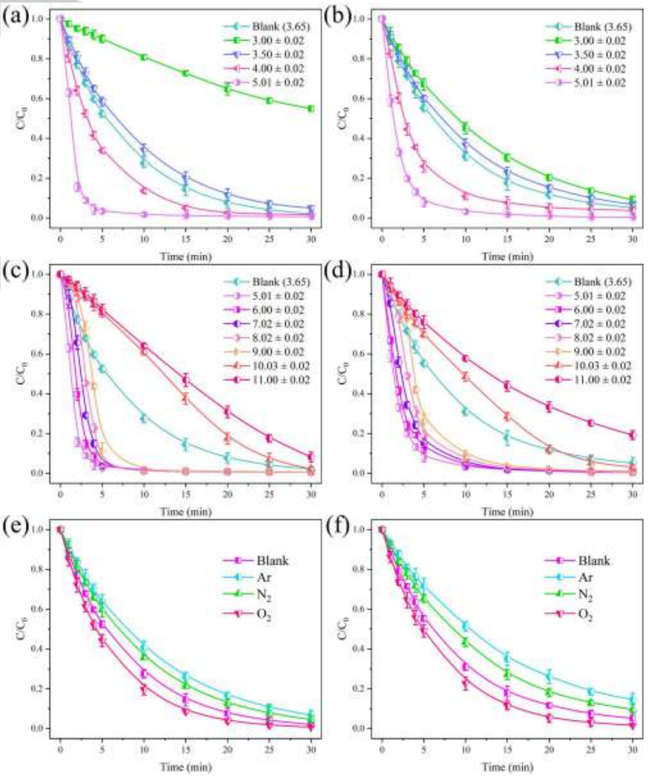

Figure 4. Effects of solution pH and continuous purge with different atmosphere on DPPA system for synergistic decontamination: (a, c, e) EB and (b, d, f) TC. Conditions: $[PMS]_0 = 0.40$ mM, $[EB]_0 = 0.02$ mM, $[TC]_0 = 10$ mg/L, $\lambda > 420$ nm irradiation, pH = 3.00 ~ 11.00 for (a - d) and pH = 3.65 for (e - f).

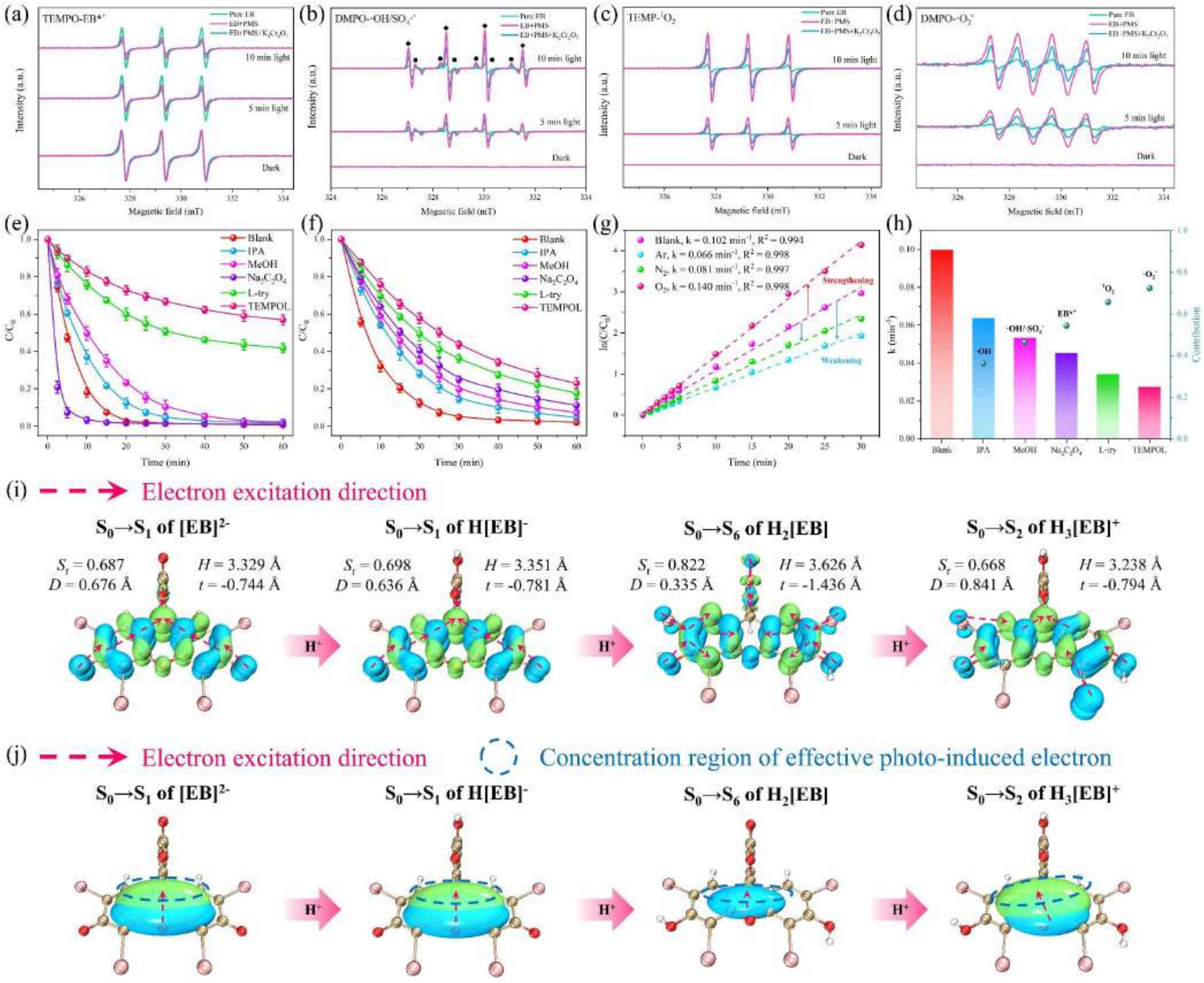

Figure 5. Stepwise analysis of reactive species and reaction mechanisms. ESR spectra of each reactive specie in DPPA system under VL irradiation, including (a) $EB^{•+}$, (b) $SO_4^{·-}$ (black solid circle) and ·OH (black solid square), (c) $^1O_2$ and (d) $·O_2^-$. EB consumption curves (e) and TC degradation curves (f) of DPPA system with different quenchers, as well as the corresponding kinetic constants of TC degradation and relative contributions of different RS (h). Kinetic curves of TC degradation under continuous Ar/N_2/O_2 purge (g). The visualization distribution (i) and C_{hole}/C_{ele} (j) analysis of electrons and holes in dominant excitation processes of EB (isosurface value: 0.0015 a.u.). The blue and green represented the holes and electrons, respectively. Conditions: $[PMS]_0$ = $[K_2Cr_2O_7]_0$ = 0.40 mM, $[EB]_0$ = 0.02 mM, $[TC]_0$ = 10 mg/L, pH = 3.65 and λ > 420 nm irradiation.

Taking $H[EB]^-$ (the main existence form under mild operating conditions) as an example, HOMO occupied the dominant position in the generation of holes with the contribution of 96.6 %, while electrons were almost composed of LUMO (97.4 %). From the perspective of atomic contribution, both electrons and holes possessed significant delocalization characteristics. The C atoms (C1 ~ C13) in conjugated systems contributed to both electrons and holes. And atoms containing lone pair electrons (I32 ~ I35, O29 and O31) mainly made contributions to 'hole' region, forming non-bonding orbitals (n), while the O30 in delocalization system contributed to 'electron' region, participating in the generation of antibonding orbitals (π^*). Moreover, charge density difference (CDD) reflected the absolute/net contribution of atoms to holes and electrons. Similarly, other excitation processes could be analyzed accordingly. It was not difficult to find that the photo-induced electrons were principally concentrated in C7 position of IDR structures, and the $EB^{•+}$ would be immediately produced after losing photoelectrons. In conclusion, during the reaction process, the electron acceptors (PMS/O_2) in DPPA system would obtain photoelectrons from the green isosurface sites in Figure 5i to form ROS and $SO_4^{·-}$, while the remaining blue isosurface regions in molecules would be transformed into the oxidation centers of $EB^{•+}$, playing roles in attacking contaminants.

Achieving the high mineralization of contaminants has always been the pursuit of effective AOPs. To better prove the efficiency of DPPA system and clarify the oxidation pathways of TC, the transformation products were identified by using UPLC-

HRMS. The mass spectra of samples at different reaction times were obtained (Figure S13), and the chemical structure of TC was illustrated in Figure S14. Based on the identified intermediates and previous research results [36], the oxidative degradation processes of TC in DPPA system were summarized into three stages (depicted in Figure S15): i) primary oxidation, ii) secondary oxidation and iii) final mineralization. Table S15 listed the intermediates that may be produced during TC degradation, and the transformation processes of intermediate products were analyzed in detail in Text S8. The results of total organic carbon (TOC) and ion chromatography (IC) analysis (Figure S16 and S17) also confirmed the decontamination advantages of DPPA system, and the mineralization rate in 30 min was as high as 50.5 %. To further verify the degradation pathways proposed in Figure S16, the OW Fukui index of TC molecule was studied based on DFT calculations and presented in Table S16. In this analysis, OW DD was mainly used to measure the reactivity of different sites, and the sites with higher absolute values were more likely to be attacked by active species [26, 37]. The corresponding analysis was listed in Text S9. These theoretical results effectively supported the inference about the degradation pathways of TC in DPPA system.

Conclusion

Developing sustainable water purification processes was urgently desired to address environmental issues caused by emerging contaminants. Here, EB was selected as the model xanthene structure to construct the sustainable DPPA system, and the photo-induced transformation of PMS in photosensitive dye-enriched solution was observed under simulated solar irradiation. The results displayed that the photo-induced electron transfer between EB^* and PMS triggered the efficient activation of PMS and significantly enhanced the production of ROS and $SO_4^{\cdot-}$. Through ESR and quenching experiments, it was confirmed that $\cdot O_2^-$, $^1O_2$ and EB^{*+} were the core reactive species, while $SO_4^{\cdot-}/\cdot OH$ may mainly participate in the mutual transformations among various active species and play a role in partial oxidation. Based on DFT calculations and photochemical behavior analysis, it was proved that PTP was the crucial factor to determine the reactivity of DPPA system, mainly leading to the ISR and IDR of dye molecules. A comprehensive hole-electron analysis based on TDDFT was carried out to reveal the reactive centers of dye molecules for PMS activation. Analysis results also indicated that the dominant excitation process was composed of the low energy excitations, and the electrons and holes were almost contributed by LUMO and HOMO. Intriguingly, the impact of PTP on DPPA system exhibited a significant dual effect on key substances and promoted the system to show high benefits in a wide range of pH. Overall, our work proposed a new method for synergistic decontamination by activating PMS under visible light, providing a practical and economical idea for the construction of eco-friendly catalyst-free synergistic decontamination process.

Acknowledgements

This study was financially supported by the program for the National Natural Science Foundation of China (52170162, 51809090, U20A20323, 51521006, 51879101), the Natural Science Foundation of Hunan Province, China (2022JJ10016, 2019JJ50077), the Science and Technology Innovation Program of Hunan Province (2021RC3049, 2020RC4014), and the Fundamental Research Funds for the Central Universities (531118010114).

Conflict of Interest

The authors have no conflict of interest to declare.

Data Availability Statement

The data that support the findings of this study are available from the corresponding author upon reasonable request.

Keywords: Advanced oxidation • Photochemistry • Catalyst-free • Environmental chemistry • Proton transfer process.

[1] a) Z. Wang, E. Almatrafi, H. Wang, H. Qin, W. Wang, L. Du, S. Chen, G. Zeng, P. Xu, *Angew. Chem. Int. Ed.* **2022**, *61*, e202202338; b) Z.-Y. Guo, Y. Si, W.-Q. Xia, F. Wang, H.-Q. Liu, C. Yang, W.-J. Zhang, W.-W. Li, *Proc. Natl. Acad. Sci.* **2022**, *119*, e2201607119.

[2] a) J. Lee, U. von Gunten, J.-H. Kim, *Environ. Sci. Technol.* **2020**, *54*, 3064-3081; b) Y.-Y. Ahn, J. Choi, M. Kim, M. S. Kim, D. Lee, W. H. Bang, E.-T. Yun, H. Lee, J.-H. Lee, C. Lee, S. K. Maeng, S. Hong, J. Lee, *Environ. Sci. Technol.* **2021**, *55*, 5382-5392.

[3] a) J. Nie, J. Zou, S. Yan, W. Song, *Environ. Sci. Technol.* **2022**, *56*, 1963-1972; b) F. Chen, L.-L. Liu, J.-J. Chen, W.-W. Li, Y.-P. Chen, Y.-J. Zhang, J.-H. Wu, S.-C. Mei, Q. Yang, H.-Q. Yu, *Water Res.* **2021**, *191*, 116799; c) L. Wei, J. Li, C. Zhou, B. Song, F. Qin, W. Wang, H. Luo, D. Qin, C. Huang, C. Zhang, Y. Yang, *Chin. Chem. Lett.* **2022**, 107893.

[4] S. Jorfi, B. Kakavandi, H. R. Motlagh, M. Ahmadi, N. Jaafarzadeh, *Appl. Catal., B* **2017**, *219*, 216-230.

[5] Z. Wei, F. A. Villamena, L. K. Weavers, *Environ. Sci. Technol.* **2017**, *51*, 3410-3417.

[6] S. Liu, C. Lai, X. Zhou, C. Zhang, L. Chen, H. Yan, L. Qin, D. Huang, H. Ye, W. Chen, L. Li, M. Zhang, L. Tang, F. Xu, D. Ma, *Water Res.* **2022**, *221*, 118797.

[7] a) B. Ma, C. Martín, R. Kurapati, A. Bianco, *Chem. Soc. Rev.* **2020**, *49*, 6224-6247; b) J. Sanchís, M. Olmos, P. Vincent, M. Farré, D. Barceló, *Environ. Sci. Technol.* **2016**, *50*, 961-969.

[8] Y. Wen, C.-H. Huang, D. C. Ashley, D. Meyerstein, D. D. Dionysiou, V. K. Sharma, X. Ma, *Environ. Sci. Technol.* **2022**, *56*, 2626-2636.

[9] a) H.-i. Kim, Y. Choi, S. Hu, W. Choi, J.-H. Kim, *Appl. Catal., B* **2018**, *229*, 121-129; b) L. Wang, D. W. Shaffer, G. F. Manbeck, D. E. Polyansky, J. J. Concepcion, *ACS Catal.* **2020**, *10*, 580-585.

[10] a) E. C. Ryberg, C. Chu, J.-H. Kim, *Environ. Sci. Technol.* **2018**, *52*, 13361-13369; b) Y. Liu, W. Dong, S. Shen, F. Meng, J. Wang, K. Yang, D. Lin, *Water Res.* **2022**, *212*, 118125.

[11] a) M. S. Frei, P. Hoess, M. Lampe, B. Nijmeijer, M. Kueblbeck, J. Ellenberg, H. Wadepohl, J. Ries, S. Pitsch, L. Reymond, K. Johnsson, *Nat. Commun.* **2019**, *10*, 4580; b) Y. Wang, J. Li, Z. Zhou, R. Zhou, Q. Sun, P. Wu, *Nat. Commun.* **2021**, *12*, 526.

[12] S. W. Benson, *Chem. Rev.* **1978**, *78*, 23-35.

[13] M. C. DeRosa, R. J. Crutchley, *Coord. Chem. Rev.* **2002**, *233-234*, 351-371.

[14] J. Ma, W. Song, C. Chen, W. Ma, J. Zhao, Y. Tang, *Environ. Sci. Technol.* **2005**, *39*, 5810-5815.

[15] S. Srisantitham, M. Sukwattanasinitt, S. Unarunotai, *Colloids Surf., A* **2018**, *550*, 123-131.

[16] V. R. Batistela, D. S. Pellosi, F. D. de Souza, W. F. da Costa, S. M. de Oliveira Santin, V. R. de Souza, W. Caetano, H. P. M. de Oliveira, I. S. Scarminio, N. Hioka, *Spectrochim. Acta, Part A* **2011**, *79*, 889-897.

[17] D. Snigur, M. Fizer, A. Chebotarev, O. Lukianova, O. Zhukovetska, *Dyes Pigm.* **2022**, *198*, 110028.

[18] F. L. Hirshfeld, *Theor. Chim. Acta* **1977**, *44*, 129-138.

[19] X. Li, X. Gao, W. Shi, H. Ma, *Chem. Rev.* **2014**, *114*, 590-659.

[20] D. Margulies, G. Melman, A. Shanzer, *Nat. Mater.* **2005**, *4*, 768-771.

[21] O. Valdes-Aguilera, D. C. Neckers, *Acc. Chem. Res.* **1989**, *22*, 171-177.

[22] Y. Urano, M. Kamiya, K. Kanda, T. Ueno, K. Hirose, T. Nagano, *J. Am. Chem. Soc.* **2005**, *127*, 4888-4894.

[23] C. Adamo, D. Jacquemin, *Chem. Soc. Rev.* **2013**, *42*, 845-856.

[24] a) Y. Yang, J. Jiang, X. Lu, J. Ma, Y. Liu, *Environ. Sci. Technol.* **2015**, *49*, 7330-7339; b) Y. Zhou, J. Jiang, Y. Gao, S.-Y. Pang, J. Ma, J. Duan, Q. Guo, J. Li, Y. Yang, *Water Res.* **2018**, *138*, 56-66.

[25] T. Cai, Y. Liu, L. Wang, W. Dong, H. Chen, W. Zeng, X. Xia, G. Zeng, *Chem. Eng. J.* **2019**, *375*, 122070.

[26] R. Pino-Rios, D. Inostroza, G. Cárdenas-Jirón, W. Tiznado, *J. Phys. Chem. A* **2019**, *123*, 10556-10562.

[27] G. Fang, J. Gao, C. Liu, D. D. Dionysiou, Y. Wang, D. Zhou, *Environ. Sci. Technol.* **2014**, *48*, 1902-1910.

[28] P. Chen, L. Blaney, G. Cagnetta, J. Huang, B. Wang, Y. Wang, S. Deng, G. Yu, *Environ. Sci. Technol.* **2019**, *53*, 1564-1575.

[29] Y. Zhou, C. Zhang, D. Huang, W. Wang, Y. Zhai, Q. Liang, Y. Yang, S. Tian, H. Luo, D. Qin, *Appl. Catal., B* **2022**, *301*, 120749.

[30] C. Zhang, Y. Zhou, W. Wang, Y. Yang, C. Zhou, L. Wang, L. Lei, D. He, H. Luo, D. Huang, *Appl. Surf. Sci.* **2020**, *527*, 146757.

[31] R. E. Huie, C. L. Clifton, N. Altstein, *Int. J. Radiat. Appl. Instrum.* **1989**, *33*, 361-370.

[32] Z. Liu, T. Lu, Q. Chen, *Carbon* **2020**, *165*, 461-467.

[33] X. Tang, L.-S. Cui, H.-C. Li, A. J. Gillett, F. Auras, Y.-K. Qu, C. Zhong, S. T. E. Jones, Z.-Q. Jiang, R. H. Friend, L.-S. Liao, *Nat. Mater.* **2020**, *19*, 1332-1338.

[34] Y. Li, L. Yang, H. He, L. Sun, H. Wang, X. Fang, Y. Zhao, D. Zheng, Y. Qi, Z. Li, W. Deng, *Nat. Commun.* **2022**, *13*, 1355.

[35] T. Lu, F. Chen, *J. Comput. Chem.* **2012**, *33*, 580-592.

[36] a) C. Liu, H. Dai, C. Tan, Q. Pan, F. Hu, X. Peng, *Appl. Catal., B* **2022**, *310*, 121326; b) L. Ge, Y. Yue, W. Wang, F. Tan, S. Zhang, X. Wang, X. Qiao, P. K. Wong, *Water Res.* **2021**, *198*, 117149.

[37] W. Yang, R. G. Parr, *Proc. Natl. Acad. Sci.* **1985**, *82*, 6723-6726.

Entry for the Table of Contents

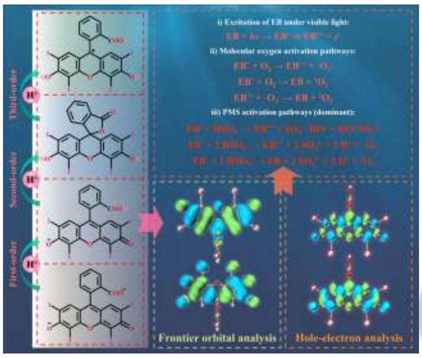

A sustainable DPPA system for synergistic decontamination was proposed through selecting EB with xanthene structure as the model dye. The photo-electron transfer between excited dye and PMS triggered the activation process and significantly enhanced the production of reactive species. It was proved that the PTP was the crucial factor to determine the reactivity of DPPA system, mainly leading to the ISR and IDR of dye molecules.